Breaking the Measurement-Sensitivity–Maximum-Range Limit of Quantum Metrology Using Two Sequences

Yang Dong,[1,2] Ce Feng,[1,2] Shao-Chun Zhang,[1,2] Yu Zheng,[1,2] Xiang-Dong Chen,[1,2] Guang-Can Guo,[1,2] and Fang-Wen Sun[1,2,*]

[1] *CAS Key Laboratory of Quantum Information, University of Science and Technology of China, Hefei 230026, People's Republic of China*

[2] *CAS Center for Excellence in Quantum Information and Quantum Physics, University of Science and Technology of China, Hefei 230026, People's Republic of China*

(Received 22 February 2022; revised 11 December 2022; accepted 16 May 2023; published 7 June 2023)

In precision measurement and quantum metrology, the 2π periodicity inherent to any interferometric signal sets a fundamental limit in the simultaneous achievement of both high measurement sensitivity and range. Here, based on the extended period of the Lissajous curve, we develop a method to break this sensitivity–maximum-range limit completely. In the measurement of magnetic field using an electronic spin in diamond under ambient conditions, we extend the maximum range by 2 orders of magnitude without sacrificing detection sensitivity and bandwidth for sufficiently long measurement time. Furthermore, we achieve precise detection of a time-varying periodic waveform, where a large measurement range can induce high accuracy and demonstrate a Heisenberg-like scaling within the coherent regime. This Lissajous-curve-based range extension method can be directly applied to any other modulo-limited quantum interferometers, which makes a useful and indispensable stepping stone toward practical interferometric quantum metrology.

DOI: 10.1103/PhysRevApplied.19.064022

I. INTRODUCTION

An interferometer is a powerful tool for measurement, which has been well adopted in applications ranging from classical precision measurement [1–10] to quantum metrology [11–13]. Currently, simultaneous optimization of measurement sensitivity (S) [14–16], maximum range [17,18], and bandwidth [19–21] is a key challenge in those interferometer-based measurements. However, the unambiguous maximum allowed field range is fundamentally limited to intrinsic 2π radians [22–27], which puts a fundamental limit on the sensitivity [12,17,18,27,28]. It also prevents precise detection of an unknown temporal profile of a time-varying waveform with a large variation amplitude [29–32]. Therefore, breaking this limit is ambitious propositions [12] both in basic researches and practical applications.

Recently, some methods have been proposed to resolve the above stumbling block in physical field measurement [12,33–35], including the exponential increase of range with a multiqubit state [36]. Moreover, both nonadaptive [17,18,23,24,26,37] and adaptive [27,38,39] quantum phase estimation algorithms were applied to break this limit with limited measurement sensitivity or bandwidth. A geometric phase interferometer [28] was also introduced. Unfortunately, it needs a rigorous periodic coherent driving continuously and precise numerical derivative information of the detection signal, which will inevitably lead to discrete measurement values and greatly increase errors in practice [16,28,40]. Moreover, the above protocols are inefficient at sampling and reconstructing time-varying signal. Based on simultaneous operation of two interferometers with different free-precession times, the 2π phase ambiguity can be removed within an enhanced range, determined by moiré or beat pattern [35], which is inversely proportional to the difference scale factor. But the free-precession times should be nearly identical. Recently, by using a set of measurement sequences, an algorithm method is proposed for high-range dc and ac magnetic field detection while retaining the best possible sensitivity [41]. However, implementation of multiple subsequences will be cumbersome for practical application.

In this paper, we engineer only an additional measurement in the interferometer, where the output can present a Lissajous curve (LC). Currently, LC has been used in various engineering applications such as optics [42], imaging [43], scanning antenna [44], machining, as well as mobile robotics [45]. Here, based on the intrinsic property of LC, we can break the sensitivity-maximum range limit by extending the range without sacrificing detection

*fwsun@ustc.edu.cn

sensitivity and bandwidth. Experimentally, we apply this method with a solid spin in diamond for both dc and ac magnetic field measurement and achieve 2 orders of magnitude enhancement in measurement range for long enough measurement times. We also successfully realize precise detection of a periodic waveform and demonstrate that large allowed range can reduce the measurement uncertainty of accumulation phase and yield a Heisenberg-like scaling within the coherent regime.

II. LC-BASED METHOD

As shown in Fig. 1(a), we consider measuring a physical parameter, such as magnetic field B, with a Ramsey interferometry [11,28,46]. The detected signal changes with the magnetic field as $P_1 = (1 + \cos\varphi_1)/2$, where $\varphi_1 = \gamma B\tau_1$. Here γ denotes the gyromagnetic ratio, and τ_1 is the interaction time with B. Figure 1(c) shows the signal value of P_1 corresponding to infinite degenerate φ_1 and B. It leads to phase unambiguity in $[0, \pi)$. Hence, the accessible field range of magnetic field detection is limited to $B_{\max} = \pi/\gamma\tau_1$. By combining with the quadrature phase detection [47] result of $P_2 = (1 + \sin\varphi_1)/2$, φ_1 within 2π can be distinguished, as shown in Fig. 1(d). However, the sensitivity [12,14], which is limited by shot noise, is restricted by the interaction time, $S \propto 1/\sqrt{\tau_1}$ for $\tau_1 < T_2^*/2$. For $\tau_1 > T_2^*/2$, it becomes exponentially worse. To break above limitation, we add a second interaction time. As shown in Fig. 1(b), the alternative interferometer with interaction time τ_2 outputs $(P_3, P_4) = ((1 + \cos\varphi_2)/2, (1 + \sin\varphi_2)/2)$. By combining P_1 and P_3, those degenerate values of φ_1 (shown with red dots) in Fig. 1(c) can be well separated in Fig. 1(e), which indicates the successful extension of unambiguous phase determination far beyond 2π.

The signals from those Ramsey interferences together with increasing magnetic field amplitude can be mapped in a two-dimensional Lissajous or Bowditch curve, as shown Figs. 1(f)–1(h). And the intrinsic property of LC can be used to construct an efficient and feasible measurement protocol without the above sensitivity-maximum range limit. Generally, LC can be described by a system of parametric equations

$$x = x_0 \sin(\gamma B\tau_1 + \phi_1),$$
$$y = y_0 \sin(\gamma B\tau_2 + \phi_2), \tag{1}$$

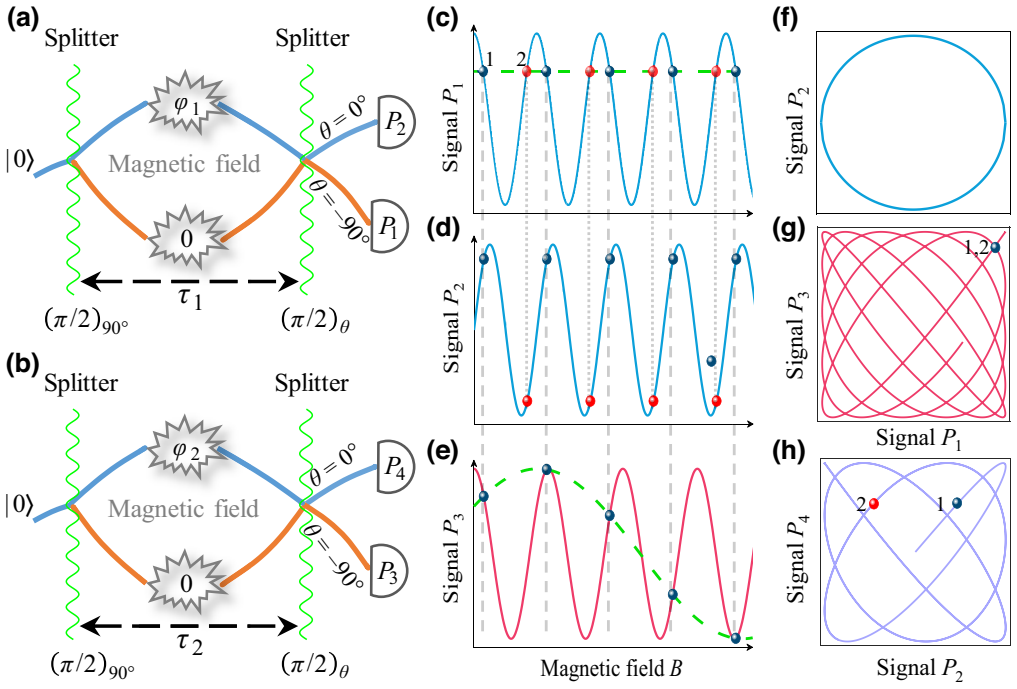

FIG. 1. Protocol of LC-based range extension on a Ramsey interferometry. (a),(b) Detecting a magnetic field with different interaction times. The probe qubit is prepared to $(|0\rangle + |1\rangle)/\sqrt{2}$ by a $\pi/2$ gate. After interaction with the magnetic field with time τ_1 (τ_2), another $\pi/2$ gate with or without a -90^0 phase shift is applied to obtain detection results of P_1 (P_3) or P_2 (P_4), respectively. (c)–(e) Signals of P_1, P_2, and P_3. In (c), blue and red points are degenerate and the phase is unambiguous in $[0, \pi)$. By comparing P_1 and P_2, blue and red points in P_1 are separated. Degenerate red points in P_1 are further distinguished by comparing P_1 and P_3 to extend the phase unambiguous range far beyond 2π. (f)–(h) LCs plotted with (P_1, P_2), (P_1, P_3), and (P_2, P_4), respectively. In (g), the blue point of intersection, corresponding to some degenerate values, can be separated with the combination of (P_2, P_4) as shown in Fig. 1(h).

where x_0 (y_0) and $\phi_{1(2)}$ denote amplitude and phase, respectively. B is an independent variable, such as the magnetic field to be detected. Here we define $\alpha = \tau_2/\tau_1$. Since the two equations contain six parameters, the curve is usually quite complicated, except in some special cases: (1) if $\alpha = 1$ and $\phi_1 = \phi_2$, we have $y = (y_0/x_0)x$. The equation shows a straight line; (2) if $\alpha = 1$ and $\phi_1 - \phi_2 = \pi/2$, we get $x^2/x_0^2 + y^2/y_0^2 = 1$, which represents an ellipse with axes along x and y axis. If in addition $x_0 = y_0$, the ellipse becomes a circle, as shown in Fig. 1(f); (3) if $\alpha \neq 1$, the curve is much more complex, as shown in Figs. 1(g) and 1(h) with $\alpha = 11/13$ and $\phi_1 = \phi_2 = \pi/2$. As long as the ratio α is a rational number, the curve—no matter how complex—will eventually repeat itself, causing the curve to be periodic. To ensure that all dimensions loop over an integer amount of times, the alternative minimum period is $2\pi/\mathrm{GCD}(\gamma\tau_1, \gamma\tau_2)$ [41], where GCD is short for greatest common divisor; (4) if α is an irrational number, the curve will never retrace its own path, resulting in a nonperiodic motion. However, as time progresses the curve will gradually fill the rectangle bounded by the rectangle $[-x_0, x_0] \times [-y_0, y_0]$.

In the determination of the measurement phase value, it is the periodicity of LC that induces degenerate results and hence limits the maximum allowed field range. For example, the phase in Fig. 1(f) is limited in 2π [28], respectively. However, by choosing a rational number α, we can extend the maximum allowed field range by $G = \max[\tau_1/\mathrm{GCD}(\tau_1, \tau_2), \tau_2/\mathrm{GCD}(\tau_1, \tau_2)]$ times automatically. Moreover, when α is an irrational number, LC will never repeat itself and completely break the periodicity of the original detection signal, although an infinite measurement time would be required. There are no restrictions on the values of τ_1, τ_2, respectively. The dynamic rang (DR) is then given by the maximum allowed range divided by the worst sensitivity. Hence, as the maximum allowed field range increases, DR can be significantly enhanced without reducing measurement sensitivity by choosing $\alpha \sim 1$ in the experiment.

III. EXPERIMENTS

In our experiment, the diamond sample with single nitrogen-vacancy (N-V) centers is mounted at the focus of a homebuilt scanning confocal microscope, which is the same as the one described in Ref. [21]. A dry objective lens (NA = 0.95 Olympus) focuses the laser onto a single N-V center and collects the emission photons. After going through a long-pass filter (Semrock BLP01-647R-25), emission photons (wavelength ranging from 647 to 800 nm) are collected into a fiber and detected using the single-photon counting module (Excelitas Technologies SPCM-AQRH-W5-FC), with a counting rate of 65 kHz and a signal-to-noise ratio of 65 : 1. The spin-1 electron spin system of the N-V center consists of degenerate $|m_s = \pm 1\rangle$ levels and a $|m_s = 0\rangle$ level, which are mutually split in energy by the zero-field splitting. A bias magnetic field (38.2 mT) aligned with the N-V axis is added to split the degenerate spin states, allowing selective addressing of the transition. Then we encode the spin sublevels $|m_s = +1\rangle$ and $|m_s = 0\rangle$ as a probe qubit. We study naturally occurring N-V centers several microns deep in the bulk diamond. The N-V spin coherent lifetimes are $T_2^* \sim 10$ μs, and $T_2 \sim 640$ μs at room temperature, respectively.

A 10-μm-diameter copper wire above the bulk diamond is used for the delivery of microwave (MW) and arbitrary waveform to the N-V center. The driving MW is generated by an arbitrary waveform generator (AWG, Keysight M8190a) and amplified by a microwave amplifier (Mini-circuits ZHL-5W-2G-S+). By adjusting the phase and duration of MW, we can realize universal quantum state operation [48,49] based on the Rabi frequency of $\Omega_R = 12.5(2)$ MHz. dc or ac signal is directly generated by another AWG (Keysight 33522B). Optical, MW, and rf pulse sequences are synchronized by a multichannel pulse generator (Spincore, PBESR-PRO-500). In the experiment, the detection signal, which is related to the population distributions between $|m_s = 0\rangle$ and $|m_s = +1\rangle$ states of the N-V center, can be converted to the successful probability of quantum coherent operation by a linear transformation.

We demonstrate the LC-based method to detect a dc magnetic field with an electron spin of N-V center in diamond [16,48–51]. It is a challenge to experimentally realize an irrational α with current digital control technology. Here, we choose $\alpha = 5/7$ with measurement durations of $\tau_1 = 2.8$ μs and $\tau_2 = 2$ μs. Figures 2(a) and 2(b) show the experimental results of (P_1, P_2) and (P_3, P_4) with the increasing magnetic field B, respectively. Experimental data of Ramsey interferometer can be fitted using a helical gray dashed curve. As shown in Fig. 2(a), P_1 is degenerate for the seven points along the green line. In Fig. 2(b), these seven values can be distinguished, as illustrated with a green helical curve [28]. The combination of experimental results are LCs, as illustrated in Figs. 2(c) and 2(d). The three sets of degenerate results in Fig. 2(c) can be resolved in Fig. 2(d). Figure 2(e) shows traditional Ramsey interferometer results. The green line depicts the seven values in Fig. 2(a), which are distinguished in Fig. 2(f). For a standard Ramsey interferometer measurement, the usually reported measurement uncertainty is only true for a single magnetic field amplitude at infinite measurement time, but otherwise, it is worse and inhomogeneous. Moreover, by employing our LC-based measurement, which has their measured signals $\pi/2$ apart, the uncertainty becomes more homogeneous as shown in Figs. 2(a) or 2(b). The homogeneity is improved further by increasing the number of phases [41]. From Figs. 2(e) and 2(f), the maximum accessible field range is enhanced by a factor of 7 with out

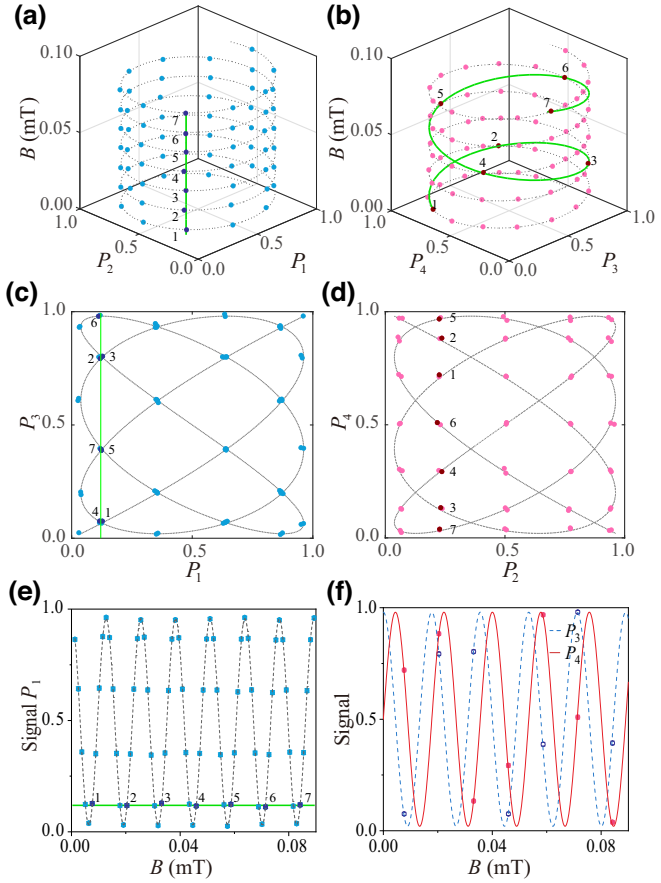

FIG. 2. Measurement of dc signal with the LC-based method. (a),(b) Results of Ramsey interferometers with different measurement durations $\tau_1 = 2.8$ μs and $\tau_2 = 2$ μs, respectively. The length of the optical readout and waiting time for single N-V center initialization is 4.5 μs. The minimum detectable magnetic field is given by $\delta B = \sigma_S/\gamma\tau R(\tau)$, where σ_S denotes error bar and $R(\tau)$ is the curvature radius of the helical line and is independent of the unknown magnetic field as shown in (a) or (b). The 7 deep blue circles along the solid green line in (a) show 2π phase ambiguity in traditional magnetometry. (c),(d) Parts of measurement results ((P_1, P_3) or (P_2, P_4)) in the same coordinate system show LCs naturally. The 3 sets of degenerate results in (c) are resolved in (d). (e) Results of P_1 against B. 2π phase ambiguity corresponds to $B_{\max} = 12.8$ μT. (f) The period of signals P_3 and P_4 is 17.8 μT. The phase accumulation rates of signals in (e), which is proportional to sensing time, is faster than the signals in (f). The different phase accumulation rates among measurement sequences are the key of our LC-based method. The maximum allowed field range that can be determined unambiguously is extended by 7 times to $B_{\max} = 89.3$ μT.

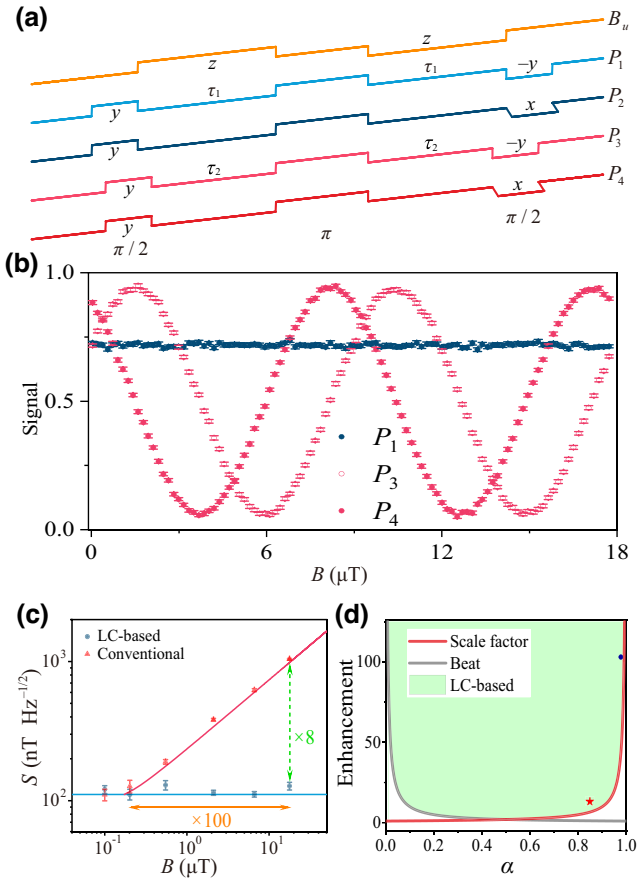

FIG. 3. Measurement of ac signal. (a) Pulse diagrams. x, $\pm y$, and z denote directions of the quantum gates in the Bloch sphere. The square-wave magnetic field is turned on for the first τ_1, turned off for π pulse, and turned on with a reverse sign for the second τ_2. The $\pi/2$ pulses for P_3 and P_4 are applied while the field is turned on. And we employ the composite-pulse technology [21] to mitigate the detuning effect of the square-wave magnetic field. (b) The degenerate amplitude of ac magnetic field measured with $2\tau_1 = 206$ μs (P_1 measurement, blue dots) are separated in the measurement with $2\tau_2 = 202$ μs (P_3 and P_4 measurements, red dots). The unknown magnetic field B can be directly calculated from quadrature detection results with Eq. (A1). (c) The sensitivity–maximum-range relationship of conventional measurement (red dots and line) is broken with the LC-based method (blue dots and line). (d) Range enhancement coefficient with different extension methods. Green region denotes feasible range enhancement coefficients with the LC-based method. Red star (blue dot) denotes experiment results in dc (ac) magnetic field measurement. Once $\alpha = 0.5$, the beat method and scale-factor method will have same effect in the improvement of the measurement range.

sacrificing detection sensitivity, compared with the original quantum interferometer.

In the detection of an ac magnetic field, our LC-based method can be combined with the dynamical decoupling (DD) method [52], as shown in Fig. 3(a). In the experiment, a rectangular ac magnetic field denoted with orange pulse in Fig. 3(a) is produced by an arbitrary function generator and applied along the N-V symmetry axis [31]. The slow rising edge of ac magnetic field influence on the performance of our protocol. At first, we measure it with an oscilloscope. Then we eliminate the effect of the slow rising edge by reducing the amplitude of the square waveform with a correct factor. The electron-spin state

is initialized to $(|0\rangle + |1\rangle)/\sqrt{2}$ by a $\pi/2$ gate. While the measured signal is changed, the superposition is also modulated in phase with the signal by a π pulse. The relative phase, φ, of the electron-spin superposition accumulating during the quantum lock-in sequence is measured by a final $\pi/2$ gate. By reducing interrogation time with a factor $\alpha = 101/103$, the measurement results in Fig. 3(b) demonstrate about 100 times enhancement of accessible field range. It increases the unambiguous detectable $B_{\max}$ to 18 μT at a decoherence-time-limited sensitivity of 114(5) $\text{nT} \cdot \text{Hz}^{-1/2}$ under ambient conditions. As shown in Fig. 3(c), the sensitivity of the standard measurement becomes worse with increasing accessible field range. This is related to the decrease of quantum sensing time τ, which in turn deteriorates $\delta B \propto \tau^{-1}$. The sensitivity of the LC-based method, however, hardly changes with increasing accessible field range. For a known magnetic field, that is, for smallest accessible field range, the DR of the standard measurement with longest sensing time $\tau \approx T_2/2$ (or $T_2^*/2$) is sufficient to achieve the highest sensitivity and to be unambiguous at the same time. But if the prior information about the magnetic field decreases, that is, accessible field range increases, the maximum range of the standard measurement is too small to maintain the highest sensitivity while staying unambiguous at the same time. Obviously, the maximum range of the LC-based method increases for increasing accessible field range while retaining the best measurement sensitivity for sufficiently long measurement times. Compared with the traditional measurement, the sensitivity is improved by about 8 times at $B_{\max} = 18$ μT. Clearly, this result breaks the sensitivity-maximum range limit, which is shown with the red line in Fig. 3(c).

IV. DISCUSSION

There is a so-called scale-factor method [33] to yield high sensitivity and range with two interrogation times, which is popular in atom interferometer systems. The longer interrogation time (τ_1) presents a greater detection sensitivity, while the shorter interrogation time (τ_2, $\alpha < 1$) shows a larger measurement range. The range enhancement coefficient is $1/\alpha$. Furthermore, when $\alpha \sim 1$, the two interferometers have slightly different scale factors. When $\alpha \sim 1$, which means two interferometers with slightly different scale factors, one can construct a beat frequency signal to extend the range in experiment [34,35]. The maximum range of a quantum interferometer can be extended by the inverse of the difference between the two interrogation times, that is $|1-\alpha|^{-1}$. Since by properly combing the measurement results, the interferometric results can be mapped onto a beat signal $y_b(P_1, P_2, P_3, P_4) = \cos(1-\alpha)\gamma B\tau \propto \left(P_1 - \frac{1}{2}\right)\left(P_3 - \frac{1}{2}\right) + \left(P_2 - \frac{1}{2}\right)\left(P_4 - \frac{1}{2}\right)$ in a rigorous way. This mapping relationship y_b is strictly continuous in mathematics. Hence, if y_b never repeats itself, one can uniquely extract independent variables (P_1, P_2, P_3, P_4) for a fixed y_b. The periodicity of y_b is less than or equal to our case. The range extension of our method is larger than the moiré or beat pattern method.

Figure 3(d) shows the theoretical results of range extension with different methods, where the LC-based method can offer higher extension coefficient than the other two methods. As shown with red star (blue dot), the LC-based range enhancement demonstrated in the measurement of dc (ac) magnetic field is much higher than that with the beat method. Also, the LC-based range extension method can be simply constructed in the experiment, which is more feasible than those range extension methods with complicated quantum algorithms or controls [17,18,28]. In the present ac magnetic field detection, we extend the range by 100 times. In principle, one can yield an arbitrary range by choosing α carefully. However, as the significant enhancement of maximum range, the same detection intensity with a serious of discrete values will become dense, and detection photon number fluctuations may lead to errors in the determination of correct unknown phase.

In experiment, one can increase the range at the cost of increasing total detection measurement resource for our protocol, such as a repeat number of experiment, the number of sensing qubits [35], and collection efficiency. In our experiment, the photon count is the immediate observable; it is directly connected to populations of the electron spin and detection signal. The population of the state $m_s = 0$ can be measured by the count r of the fluorescence detected during a second laser pulse, since the state $m_s = 0$ fluoresces more strongly than $m_s = \pm 1$ [16,48]: $r = r_{\min} + P_{|0\rangle\langle 0|}(r_{\max} - r_{\min})$. The maximum count $r_{\max}$ corresponds to the system being in state $m_s = 0$, while the minimum count rate $r_{\min}$ results when the system is in $m_s = \pm 1$. The detection signal of a single N-V center is acquired by normalizing collection photon signal with $C = r_{\max} - r_{\min}/r_{\max} \approx 0.3$. The normalized photon shot noise $\sigma_n = \sqrt{r}/rC = 1/\sqrt{I\Delta t}C$ is shown in Figs. 2 and 3 with error bars and leads a phase estimation uncertainty $\Delta\varphi$, where Δt is readout duration and I is photon counter rate. If we extend measurement range G-fold, G degenerate points should be distinguished in experiment. The average measurement uncertainty for those G points is $e^{-(\tau/T_2)^2}/G$, where τ is the interaction time with B. Then the number of the measurement repeats should satisfy $e^{-(\tau/T_2)^2}/G \sim \sigma_n/\sqrt{N}$ or $N \sim 1/I\Delta t(G/C)^2 e^{2(\tau/T_2)^2}$.

For a G-fold enhancement in measurement range, it will take a large repeat number ($N \sim (G/C)^2$) of measurements in the conventional optical readout method of the N-V center. Fortunately, different strategies are feasible to mitigate low photon collection efficiency of conventional optical readout of N-V center. By using a hemispherical diamond solid immersion lens or nanopillars, the detection signal can be enhanced by 10 times at least, which would increase

the photon-shot-noise measurement range and sensitivity by a factor of 3. And by employing single-shot readout with spin-to-charge conversion [53,54], the contrast of the detection signal can be enhanced by 3 times. The diamond crystals can be isotopically purified with ^{12}C spinless atoms during sample growth, thus reducing the content of ^{13}C to about 0.002%. Being nestled in such a spin depleting lattice, the longest coherence time of N-V is typically at the order of millisecond [55]. After taking these facts into consideration, the experimental available measurement range and sensitivity of N-V center can be enhanced by another 100 times. Moreover, in terms of our specific experiments, by choosing a series of sensing time $\tau_1, \tau_2, \tau_3, \tau_4, \cdots$, we can further improve the sensitivity by making use of N-dimensional LC in principle [41]. For example, the quantum phase estimation algorithms can be treated as a special case of N-dimensional Lissajous figure method in principle. However, no matter what experimental technology is used, it is a still untrivial challenge to decouple measurement rang and sensitivity in experiment totally.

V. APPLICATION TO WAVEFORM MEASUREMENT

Beyond the above well-established single-parameter measurement scheme, a more general task is to record a continuous time-varying periodic waveform [29,30]. In this case, the amplitude of the waveform may cover a large range and the sensitivity-maximum range contradiction direct limit the detection sensitivity. To track such a time-varying periodic signal precisely, we employ the arbitrary waveforms reconstruction-free method [31,40], as shown in Fig. 4(a). The quantum probe is initialized into $(|0\rangle + |1\rangle)/\sqrt{2}$. Then, the superposition state evolves under an unknown magnetic field $B(t)$ by accumulating a relative phase of $\varphi_1 = \int_0^{t_i} \gamma B(t)\, dt$ within $[0, t_i)$. By applying a flip π_x gate, we change the sign of the phase. Then, the probe qubit interacts with magnetic field within $[t_i, T + t_i + t_s)$ and the accumulation phase is $\varphi_2 = -\varphi_1 + \int_{t_i}^{T+t_i+t_s} \gamma B(t)\, dt$. After we change the sign of the phase with the second π_x gate, the probe qubit evolves under magnetic field within $[T + t_i + t_s, 2T)$ and the total accumulation phase is $\varphi(t_i) = -\varphi_2 + \int_{T+t_i+t_s}^{2T} \gamma B(t)\, dt \approx -2\gamma_e B(t_i) t_s$ with $t_s/T \ll 1$. Finally, by using a $(\pi/2)_\theta$ gate with $\theta = -90^\circ$ and $\theta = 0^\circ$, we get measurement results of $a_1 \cos\varphi(t_i) + 0.5$ and $a_1 \sin\varphi(t_i) + 0.5$, respectively, where a_1 denotes the amplitude of the detection signal.

By combining with the multiple passes' scheme [22], we can coherently amplify the accumulation phase $\varphi(t_i)$ by increasing repeat times k. By shrinking the sampling time (t_s) with $\alpha = 0.7$, the accessible field range can be directly extended by 10 times in theory. Figure 4(b) shows the readout of the accumulation phase from a time-varying signal recorded with different k. The accumulation

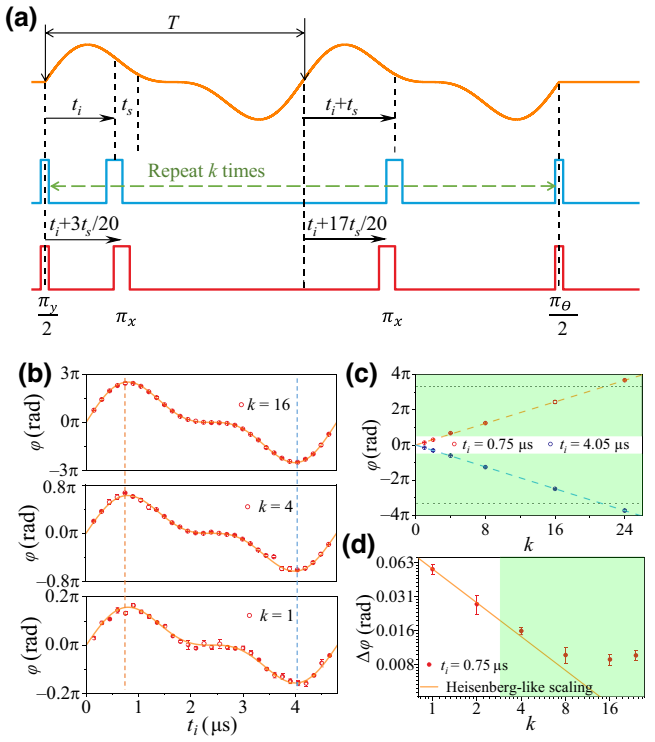

FIG. 4. High accessible field range periodic waveform measurement. (a) Pulse diagrams for time-varying waveform measurement. The basic two-π-pulse block is repeated k times to accumulate phase form $2k$ waveform passage, up to a limit set by dephasing effect. The input waveform (orange line) is $B(t) = B_0[\sin(2\pi t/T) + \sin(4\pi t/T)/2]$ with $T = 5.8$ μs. The sampling time is $t_s = 150$ ns. (b) Measurement results with a series of repeating times k. (c) The accumulation phase ($\varphi(t_i)$) with different repeat numbers at $t_i = 0.75$ μs (red) and $t_i = 4.05$ μs (blue). Black dashed lines denote accessible field range extension with the beat method. (d) Standard deviations ($\Delta\varphi$) of the accumulation phase at $t_i = 0.75$ μs. Red dots show the experimental results. The orange line represents the Heisenberg scaling in the absence of probe qubit decoherence. Green regions in (b),(c) denote the extension of the accessible field range.

phase is proportional to the repeat times at a fixed t_i. By increasing k, a much stronger oscillation response far beyond the measurement interval $[-\pi/2, \pi/2]$ is measured, as shown in Figs. 4(b) and 4(c). The green region in Fig. 4(c) denotes about 4 times accessible field range extension with our method in the experiment. Moreover, as shown in Fig. 4(d), with large accessible field range, the measurement uncertainty of accumulation phase can be reduced further, yielding a clear Heisenberg-like scaling $\Delta\varphi \propto 1/k$ in the coherent regime. Thus, the repeat number (k) is mainly limited by the dephasing time and DD method could be added during the phase accumulation time to mitigate this effect [56]. The realization of the quantum-enhancement tracking of the time-varying signal indicates that the present method is very compatible with the time-domain quantum measurement protocols

and the bandwidth is only limited by Rabi frequency [40]. However, the sensitivity for arbitrary waveforms reconstruction-free method is not high, because the most of the coherence sensing time is spent on canceling unwanted phase accumulation. If the frequency component of test signal is low (approximately < 1 kHz), the fitting-based algorithm with Ramsey sequences [57] will lead to better sensitivity in experiment.

VI. CONCLUSION

In conclusion, based on the the extended period of LC, we propose and demonstrate a method to break the trade-off between measurement sensitivity and maximum range in theory. With a single N-V center in diamond, we realize 2 orders of magnitude enhancement in measurement range at decoherence-limited sensitivity, which can be further enhanced by increasing the signal-to-noise ratio of the detection signal. The successful application to the measurement of periodic waveform shows that large accessible field range can present high detection accuracy. This LC-based method is naturally compatible in precision measurement with current physical systems, such as LIGO, atom [58], transmon [59], ultracold molecules [60], and other solid spin systems [61]. Moreover, it can be applied in the interferometer with multientangled qubits to achieve the Heisenberg limit [62,63] in quantum metrology.

ACKNOWLEDGMENTS

This work is supported by the National Key Research and Development Program of China (Grant No. 2017YFA 0304504), the National Natural Science Foundation of China (Grants No. 12005218, and No. 52130510), the Science Challenge Project (Grant No. TZ2018003), the Key Research and Development Plan of Jiangsu Province (Grant No. BE2022066-2).

APPENDIX: RAMSEY INTERFEROMETRY AND QUADRATURE DETECTION

As shown in Fig. 5(a), we outline Ramsey-type interferometry for magnetic field measurement using an N-V center in a two-level subspace, $\{|m_s = 0\rangle \equiv |0\rangle, |m_s = +1\rangle \equiv |1\rangle\}$. After initializing the N-V center into $|0\rangle$, a MW field, with polarization in the x-y plane of Bloch sphere and frequency resonant with $|0\rangle \leftrightarrow |1\rangle$, causes spin population to oscillate between the $|0\rangle$ and $|1\rangle$ states at angular frequency Ω_R. The resonant MW field is applied for a particular finite duration $\pi/2\Omega_R$, known as a $\pi/2$ pulse, which transforms the initial state $|0\rangle$ into $(|0\rangle + |1\rangle)/\sqrt{2}$. This probe state is then left to precess for duration τ, during which a magnetic field dependent phase φ accumulates between $|0\rangle$ and $|1\rangle$. Finally, a second $\pi/2$ pulse is applied, mapping the phase φ onto a population difference between $|0\rangle$ and $|1\rangle$. Figure 5(b) provides

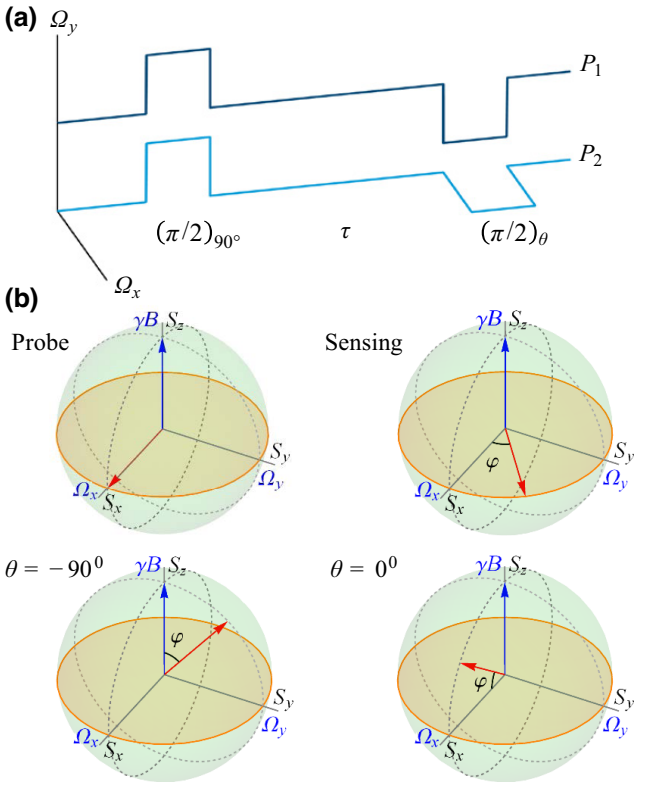

FIG. 5. Quantum interferometer for the measurement of dc signal. (a) Ramsey interferometry diagrams for dc signal measurement. (b) Bloch-sphere depiction of Ramsey measurement sequence.

a Bloch-sphere depiction of the Ramsey sequence. By using -90° and 0° phase-shifted $\pi/2$ pulse (compared with the first pulse), both cosine and sine components of the unknown phase are measured $(P_1, P_2) = (S_x, S_y) = (1 + \cos\gamma B\tau/2, 1 + \sin\gamma B\tau/2)$, which is equivalent to full quadrature detection.

The unknown magnetic field B can be directly calculated from quadrature detection results in simple way:

$$\begin{aligned} B_1 &= \frac{\arccos(2P_1 - 1) + 2k_1\pi}{\gamma\tau_1} \\ B_2 &= \frac{\arcsin(2P_2 - 1) + 2k_1\pi}{\gamma\tau_1} \\ B_3 &= \frac{\arccos(2P_3 - 1) + 2k_2\pi}{\gamma\tau_2} \\ B_4 &= \frac{\arcsin(2P_4 - 1) + 2k_2\pi}{\gamma\tau_2} \end{aligned}, \tag{A1}$$

where k_1, k_2 are positive integer numbers, arccos or arcsin is inverse trigonometric. And the restricted condition is

$$\begin{aligned} \arccos(2P_i - 1) &\in [0, 2\pi), i = 1, 3 \\ \arcsin(2P_j - 1) &\in [0, 2\pi), j = 2, 4 \\ 0 \leqslant B_k &< B_{\max}, k = 1, 2, 3, 4 \end{aligned}$$

and $B_{\max} = 2\pi/\mathrm{GCD}(\gamma\tau_1, \gamma\tau_2)$. In the experiment, there is always a slight difference between B_1 and B_2 (or B_3 and B_4) due to the statistical error of measurement. We find one set of solutions (k_1, k_2) to minimize target function $E = |B_1 - B_3| + |B_2 - B_4|$ and choose one of B_1, B_2, B_3, or B_4 with minimum uncertainty as the value of magnetic field.

[1] L. Morel, Z. Yao, P. Cladé, and S. Guellati-Khélifa, Determination of the fine-structure constant with an accuracy of 81 parts per trillion, Nature (London) **588**, 61 (2020).

[2] R. H. Parker, C. Yu, W. Zhong, B. Estey, and H. Müller, Measurement of the fine-structure constant as a test of the Standard Model, Science **360**, 191 (2018).

[3] G. Rosi, F. Sorrentino, L. Cacciapuoti, M. Prevedelli, and G. Tino, Precision measurement of the Newtonian gravitational constant using cold atoms, Nature (London) **510**, 518 (2014).

[4] Q. Li, C. Xue, J.-P. Liu, J.-F. Wu, S.-Q. Yang, C.-G. Shao, L.-D. Quan, W.-H. Tan, L.-C. Tu, and Q. Liu, *et al.*, Measurements of the gravitational constant using two independent methods, Nature (London) **560**, 582 (2018).

[5] M. Zych and Č. Brukner, Quantum formulation of the Einstein equivalence principle, Nat. Phys. **14**, 1027 (2018).

[6] L. Zhou, S. Long, B. Tang, X. Chen, F. Gao, W. Peng, W. Duan, J. Zhong, Z. Xiong, and J. Wang, *et al.*, Test of Equivalence Principle at 10^{-8} Level by a Dual-Species Double-Diffraction Raman Atom Interferometer, Phys. Rev. Lett. **115**, 013004 (2015).

[7] G. Bertone and T. M. Tait, A new era in the search for dark matter, Nature (London) **562**, 51 (2018).

[8] P. Hamilton, M. Jaffe, P. Haslinger, Q. Simmons, H. Müller, and J. Khoury, Atom-interferometry constraints on dark energy, Science **349**, 849 (2015).

[9] V. Xu, M. Jaffe, C. D. Panda, S. L. Kristensen, L. W. Clark, and H. Müller, Probing gravity by holding atoms for 20 seconds, Science **366**, 745 (2019).

[10] D. Becker, M. D. Lachmann, S. T. Seidel, H. Ahlers, A. N. Dinkelaker, J. Grosse, O. Hellmig, H. Müntinga, V. Schkolnik, and T. Wendrich, *et al.*, Space-borne Bose–Einstein condensation for precision interferometry, Nature (London) **562**, 391 (2018).

[11] K. Bongs, M. Holynski, J. Vovrosh, P. Bouyer, G. Condon, E. Rasel, C. Schubert, W. P. Schleich, and A. Roura, Taking atom interferometric quantum sensors from the laboratory to real-world applications, Nat. Rev. Phys. **1**, 731 (2019).

[12] C. L. Degen, F. Reinhard, and P. Cappellaro, Quantum sensing, Rev. Mod. Phys. **89**, 035002 (2017).

[13] M. Safronova, D. Budker, D. DeMille, D. F. J. Kimball, A. Derevianko, and C. W. Clark, Search for new physics with atoms and molecules, Rev. Mod. Phys. **90**, 025008 (2018).

[14] J. R. Maze, P. L. Stanwix, J. S. Hodges, S. Hong, J. M. Taylor, P. Cappellaro, L. Jiang, M. G. Dutt, E. Togan, and A. Zibrov, *et al.*, Nanoscale magnetic sensing with an individual electronic spin in diamond, Nature (London) **455**, 644 (2008).

[15] F. Hudelist, J. Kong, C. Liu, J. Jing, Z. Ou, and W. Zhang, Quantum metrology with parametric amplifier-based photon correlation interferometers, Nat. Commun. **5**, 3049 (2014).

[16] J. F. Barry, J. M. Schloss, E. Bauch, M. J. Turner, C. A. Hart, L. M. Pham, and R. L. Walsworth, Sensitivity optimization for NV-diamond magnetometry, Rev. Mod. Phys. **92**, 015004 (2020).

[17] G. Waldherr, J. Beck, P. Neumann, R. Said, M. Nitsche, M. Markham, D. Twitchen, J. Twamley, F. Jelezko, and J. Wrachtrup, High-dynamic-range magnetometry with a single nuclear spin in diamond, Nat. Nanotechnol. **7**, 105 (2012).

[18] N. Nusran, M. U. Momeen, and M. G. Dutt, High-dynamic-range magnetometry with a single electronic spin in diamond, Nat. Nanotechnol. **7**, 109 (2012).

[19] H. Clevenson, M. E. Trusheim, C. Teale, T. Schröder, D. Braje, and D. Englund, Broadband magnetometry and temperature sensing with a light-trapping diamond waveguide, Nat. Phys. **11**, 393 (2015).

[20] I. Jakobi, P. Neumann, Y. Wang, D. B. R. Dasari, F. El Hallak, M. A. Bashir, M. Markham, A. Edmonds, D. Twitchen, and J. Wrachtrup, Measuring broadband magnetic fields on the nanoscale using a hybrid quantum register, Nat. Nanotechnol. **12**, 67 (2017).

[21] Y. Dong, S.-C. Zhang, H.-B. Lin, X.-D. Chen, W. Zhu, G.-Z. Wang, G.-C. Guo, and F.-W. Sun, Quantifying the performance of multipulse quantum sensing, Phys. Rev. B **103**, 104104 (2021).

[22] B. L. Higgins, D. W. Berry, S. D. Bartlett, H. M. Wiseman, and G. J. Pryde, Entanglement-free Heisenberg-limited phase estimation, Nature (London) **450**, 393 (2007).

[23] B. Higgins, D. Berry, S. Bartlett, M. Mitchell, H. Wiseman, and G. Pryde, Demonstrating Heisenberg-limited unambiguous phase estimation without adaptive measurements, New J. Phys. **11**, 073023 (2009).

[24] D. W. Berry, B. L. Higgins, S. D. Bartlett, M. W. Mitchell, G. J. Pryde, and H. M. Wiseman, How to perform the most accurate possible phase measurements, Phys. Rev. A **80**, 052114 (2009).

[25] G.-Y. Xiang, B. L. Higgins, D. Berry, H. M. Wiseman, and G. Pryde, Entanglement-enhanced measurement of a completely unknown optical phase, Nat. Photon. **5**, 43 (2011).

[26] N. Nusran and M. G. Dutt, Optimizing phase-estimation algorithms for diamond spin magnetometry, Phys. Rev. B **90**, 024422 (2014).

[27] T. Joas, S. Schmitt, R. Santagati, A. A. Gentile, C. Bonato, A. Laing, L. P. McGuinness, and F. Jelezko, Online adaptive quantum characterization of a nuclear spin, npj Quantum Inf. **7**, 56 (2021).

[28] K. Arai, J. Lee, C. Belthangady, D. R. Glenn, H. Zhang, and R. L. Walsworth, Geometric phase magnetometry using a solid-state spin, Nat. Commun. **9**, 4996 (2018).

[29] A. Cooper, E. Magesan, H. Yum, and P. Cappellaro, Time-resolved magnetic sensing with electronic spins in diamond, Nat. Commun. **5**, 3141 (2014).

[30] N. Kura and M. Ueda, Standard Quantum Limit and Heisenberg Limit in Function Estimation, Phys. Rev. Lett. **124**, 010507 (2020).

[31] Y. Dong, Z.-H. Wang, H.-B. Lin, S.-C. Zhang, Y. Zheng, X.-D. Chen, W. Zhu, G.-Z. Wang, G.-C. Guo, and F.-W.

Sun, Heisenberg-limited waveform estimation with solid-state spins in diamond. (2021), ArXiv:2105.06037.

[32] I. Gianani, F. Albarelli, V. Cimini, and M. Barbieri, Experimental function estimation from quantum phase measurements, Phys. Rev. A **103**, 042602 (2021).

[33] A. Bonnin, C. Diboune, N. Zahzam, Y. Bidel, M. Cadoret, and A. Bresson, New concepts of inertial measurements with multi-species atom interferometry, Appl. Phys. B **124**, 1 (2018).

[34] K. Falaggis, D. P. Towers, and C. E. Towers, Multiwavelength interferometry: Extended range metrology, Opt. Lett. **34**, 950 (2009).

[35] D. Yankelev, C. Avinadav, N. Davidson, and O. Firstenberg, Atom interferometry with thousand-fold increase in dynamic range, Sci. Adv. **6**, eabd0650 (2020).

[36] V. Vorobyov, S. Zaiser, N. Abt, J. Meinel, D. Dasari, P. Neumann, and J. Wrachtrup, Quantum Fourier transform for nanoscale quantum sensing, npj Quantum Inf. **7**, 124 (2021).

[37] N. Nusran and M. G. Dutt, Dual-channel lock-in magnetometer with a single spin in diamond, Phys. Rev. B **88**, 220410 (2013).

[38] C. Bonato, M. S. Blok, H. T. Dinani, D. W. Berry, M. L. Markham, D. J. Twitchen, and R. Hanson, Optimized quantum sensing with a single electron spin using real-time adaptive measurements, Nat. Nanotechnol. **11**, 247 (2016).

[39] C. Bonato and D. W. Berry, Adaptive tracking of a time-varying field with a quantum sensor, Phys. Rev. A **95**, 052348 (2017).

[40] J. Zopes and C. L. Degen, Reconstruction-Free Quantum Sensing of Arbitrary Waveforms, Phys. Rev. Appl. **12**, 054028 (2019).

[41] E. Herbschleb, H. Kato, T. Makino, S. Yamasaki, and N. Mizuochi, Ultra-high dynamic range quantum measurement retaining its sensitivity, Nat. Commun. **12**, 306 (2021).

[42] A. J. Danner, H. Dao, and T. Tyc, The Lissajous lens: a three-dimensional absolute optical instrument without spherical symmetry, Opt. Express **23**, 5716 (2015).

[43] T. Tuma, J. Lygeros, V. Kartik, A. Sebastian, and A. Pantazi, High-speed multiresolution scanning probe microscopy based on Lissajous scan trajectories, Nanotechnology **23**, 185501 (2012).

[44] W. Gawronski and E. M. Craparo, Antenna scanning techniques for estimation of spacecraft position, IEEE Trans. Antennas Propag. **44**, 38 (2002).

[45] A. V. Borkar, A. Sinha, L. Vachhani, and H. Arya, Application of Lissajous curves in trajectory planning of multiple agents, Auton. Robots **44**, 233 (2020).

[46] C. Qiu, S. Chen, L. Chen, B. Chen, J. Guo, Z. Ou, and W. Zhang, Atom–light superposition oscillation and Ramsey-like atom–light interferometer, Optica **3**, 775 (2016).

[47] D. D. Traficante, Phase-Sensitive Detection. Part ii: Quadrature Phase Detection, Concepts Magn. Reson. **2**, 181 (1990).

[48] Y. Dong, Y. Zheng, S. Li, C.-C. Li, X.-D. Chen, G.-C. Guo, and F.-W. Sun, Non-Markovianity-assisted high-fidelity Deutsch–Jozsa algorithm in diamond, npj Quantum Inf. **4**, 3 (2018).

[49] Y. Dong, S.-C. Zhang, Y. Zheng, H.-B. Lin, L.-K. Shan, X.-D. Chen, W. Zhu, G.-Z. Wang, G.-C. Guo, and F.-W. Sun, Experimental Implementation of Universal Holonomic Quantum Computation on Solid-State Spins with Optimal Control, Phys. Rev. Appl. **16**, 024060 (2021).

[50] X.-D. Chen, E.-H. Wang, L.-K. Shan, C. Feng, Y. Zheng, Y. Dong, G.-C. Guo, and F.-W. Sun, Focusing the electromagnetic field to $10^{-6}\lambda$ for ultra-high enhancement of field-matter interaction, Nat. Commun. **12**, 6389 (2021).

[51] S. Castelletto and A. Boretti, Color centers in wide-bandgap semiconductors for subdiffraction imaging: a review, Adv. Photon. **3**, 054001 (2021).

[52] S. Kotler, N. Akerman, Y. Glickman, A. Keselman, and R. Ozeri, Single-ion quantum lock-in amplifier, Nature (London) **473**, 61 (2011).

[53] D. A. Hopper, H. J. Shulevitz, and L. C. Bassett, Spin readout techniques of the nitrogen-vacancy center in diamond, Micromachines **9**, 437 (2018).

[54] Q. Zhang, Y. Guo, W. Ji, M. Wang, J. Yin, F. Kong, Y. Lin, C. Yin, F. Shi, and Y. Wang, *et al.*, High-fidelity single-shot readout of single electron spin in diamond with spin-to-charge conversion, Nat. Commun. **12**, 1529 (2021).

[55] E. Herbschleb, H. Kato, Y. Maruyama, T. Danjo, T. Makino, S. Yamasaki, I. Ohki, K. Hayashi, H. Morishita, and M. Fujiwara, *et al.*, Ultra-long coherence times amongst room-temperature solid-state spins, Nat. Commun. **10**, 3766 (2019).

[56] Y. Dong, X.-D. Chen, G.-C. Guo, and F.-W. Sun, Reviving the precision of multiple entangled probes in an open system by simple π-pulse sequences, Phys. Rev. A **94**, 052322 (2016).

[57] E. Herbschleb, I. Ohki, K. Morita, Y. Yoshii, H. Kato, T. Makino, S. Yamasaki, and N. Mizuochi, Low-Frequency Quantum Sensing, Phys. Rev. Appl. **18**, 034058 (2022).

[58] B. Chen, C. Qiu, S. Chen, J. Guo, L. Chen, Z. Ou, and W. Zhang, Atom-Light Hybrid Interferometer, Phys. Rev. Lett. **115**, 043602 (2015).

[59] A. P. Place, L. V. Rodgers, P. Mundada, B. M. Smitham, M. Fitzpatrick, Z. Leng, A. Premkumar, J. Bryon, A. Vrajitoarea, and S. Sussman, *et al.*, New material platform for superconducting transmon qubits with coherence times exceeding 0.3 milliseconds, Nat. Commun. **12**, 1779 (2021).

[60] X. He, K. Wang, J. Zhuang, P. Xu, X. Gao, R. Guo, C. Sheng, M. Liu, J. Wang, and J. Li, *et al.*, Coherently forming a single molecule in an optical trap, Science **370**, 331 (2020).

[61] J.-F. Wang, F.-F. Yan, Q. Li, Z.-H. Liu, J.-M. Cui, Z.-D. Liu, A. Gali, J.-S. Xu, C.-F. Li, and G.-C. Guo, Robust coherent control of solid-state spin qubits using anti-Stokes excitation, Nat. Commun. **12**, 3223 (2021).

[62] Y. Dong, C. Feng, Y. Zheng, X.-D. Chen, G.-C. Guo, and F.-W. Sun, Fast high-fidelity geometric quantum control with quantum brachistochrones, Phys. Rev. Res. **3**, 043177 (2021).

[63] R. Liu, Y. Chen, M. Jiang, X. Yang, Z. Wu, Y. Li, H. Yuan, X. Peng, and J. Du, Experimental critical quantum metrology with the Heisenberg scaling, npj Quantum Inf. **7**, 170 (2021).